ORIGINAL RESEARCH ARTICLE

The Beneficial Effect of Iron in Aluminum-Cerium-Based Cast Alloys

MICHAEL P. MOODISPAW, EMRE CINKILIC, JIASHI MIAO, and ALAN A. LUO

Iron (Fe) has been considered a major impurity since it is detrimental to the mechanical properties of many cast aluminum alloys due to the formation of Fe-containing brittle intermetallic phases. Fe is found naturally as an impurity in bauxite ore, resulting in Fe contamination of aluminum alloys with increasing contamination from current recycling practices. The Al–Ce–Fe system was investigated using CALPHAD (CALculation of PHAse Diagrams) modeling and experimental casting techniques. It was found that additions of Fe to the Al–Ce system are beneficial to the strength (slightly) and ductility (significantly) of the ternary alloys, which is attributed to the formation of fine metastable Al_8CeFe_2 phase with aggregate morphology and equilibrium $Al_{10}CeFe_2$ phase, suppressing coarse proeutectic $Al_{11}Ce_3$ phase in near-eutectic Al–Ce alloys. Heat treatment study showed that the metastable Al_8CeFe_2 phase transforms to predicted equilibrium $Al_{10}CeFe_2$ phase at 500 °C, with essentially no intermetallic or grain coarsening; thus, the alloy displayed excellent property retention. The Al–Ce–Fe alloy system offers opportunities for sustainable, recyclable alloy development using low-cost Fe and low-cost cerium (a byproduct of rare-earth extraction).

https://doi.org/10.1007/s11661-024-07333-8
© The Author(s) 2024

I. INTRODUCTION

THE effect of iron (Fe) addition on the near-eutectic aluminum–cerium (Al–Ce) binary alloy was previously studied by the current authors to investigate the impact of high Fe impurity on the Al–Ce near-eutectic casting alloys.[1–3] The study was aimed at understanding the potential recyclability or potential for sorted scrap content to be used in the Al–Ce alloy production. Ce is the most abundant of the rare-earth (RE) elements, followed by lanthanum, with both individually being more abundant than copper in the Earth's crust.[4] Cerium is a relatively low-cost and sustainable alloying element for aluminum alloys since it is a byproduct of high-value RE metal extraction operations with limited demand from other industries.[5] Likewise, Fe is an inexpensive element and is found in high quantities in aluminum scrap streams but is generally avoided due to having unwanted effects on the mechanical properties of aluminum alloys. Fe is also an inherent impurity in aluminum alloys along with silicon (Si) due to their presence in bauxite ore used to produce 99.7 pct pure Al. Fe is known to form many different intermetallic phases in Al alloys depending on the composition and processing conditions.[6] When Si is also present, Al–Fe–Si phases usually form and are considered detrimental to the alloy ductility.[7] Several investigations into the Al–Ce binary system have shown promising high-temperature properties compared with traditional Al–Si or Al–Cu-based alloys[8–15] due to thermal stability of the $Al_{11}Ce_3$ phase which has no change in phase fraction until the melting point due to the lack of solubility of Ce in Al.[16] Very few studies have investigated the Al–Ce cast alloys with ternary Fe element.

There is some discrepancy in previous studies regarding the types of phases that exist in Al–Ce–Fe-based alloys. Ayer *et al.*[17] identified three metastable phases: Al_6Fe, $Al_{10}Fe_2Ce$, and decagonal quasicrystal $Al_{20}Fe_5Ce$ phases in as-extruded rapidly solidified (RS) A1–8.8Fe−3.7Ce* alloy. The metastable $Al_{10}Fe_2Ce$

MICHAEL P. MOODISPAW and JIASHI MIAO are with the Department of Materials Science and Engineering, The Ohio State University, Columbus, OH. EMRE CINKILIC is with the Department of Materials Science and Engineering, The Ohio State University and with the Department of Materials Science and Engineering, Hakkari University, Hakkari, Turkey. ALAN A. LUO is with the Department of Materials Science and Engineering, The Ohio State University and with the Department of Integrated Systems Engineering, The Ohio State University, Columbus, OH. Contact e-mail: luo.445@osu.edu

Manuscript submitted November 21, 2023; accepted January 19, 2024.

*All compositions in weight percent unless otherwise mentioned.

Published online: 08 March 2024

has an orthorhombic crystal structure (space group Cmm2/C222) and lattice parameters of a = 1.02 nm, b = 1.62 nm, and c = 0.42 nm.[17] After annealing at 700 K, the ternary metastable Al–Fe–Ce phases transformed into the equilibrium $Al_{13}Fe_3Ce$ phase with an orthorhombic crystal structure (Cmcm/Cmc2) and lattice parameters a = 0.89 nm, b = 1.02 nm, and c = 0.91 nm.[17] Öveçoglu *et al.*[18] reported the coexistence of metastable $Al_{10}Fe_2Ce$ phase and stable $Al_{13}Fe_3Ce$ phase in a mechanically alloyed RS A1–8.4Fe−3.4Ce alloy. In a RS Al–8.32Fe−3.4Ce alloy prepared using gas atomization and extrusion, Zhang *et al.*[19] identified metastable Al_mFe, Al_8Ce, and equilibrium $Al_{13}Fe_4$ phases in the as-extruded sample. After heat treatment at 230 °C, equilibrium $Al_{13}Fe_4$ and $Al_{13}Fe_3Ce$ phases were observed. Such discrepancies in phases may be attributed to the differences in alloy processing techniques. A recent study by Park *et al.* investigated the Al–10Ce–(1,3)Fe eutectic alloys to investigate the effect of Fe on the hardness and creep resistance of the Al–Ce near-eutectic alloy.[20] They concluded that the addition of Fe showed improvements to the alloy depending on the compositions and processing conditions. In the previously mentioned reports,[1,20] a ternary Al–Ce–Fe phase, namely $Al_{10}CeFe_2$, was identified in the near-eutectic Al–Ce alloy with Fe but only through scanning electron microcopy (SEM) and electron dispersive spectroscopy (EDS) methods. Thermodynamic predictions were used in both cases to identify $Al_{10}CeFe_2$ as the phase based on SEM-EDS measurements, but with no definitive transmission electron microcopy (TEM) identification. Since the Al–Ce alloys are being designed for high-temperature applications, the effect of heat treatment was also observed on the microstructure of the cast Al–10Ce–(1,3)Fe alloys, but no phase changes were observed. An electrical Al–Fe alloy modified by small additions of Ce was also recently investigated and $Al_{10}CeFe_2$ phase was reported.[21]

This study investigated the cast near-eutectic Al–Ce alloys with and without Fe additions. It is necessary to understand the phase formation during solidification and the effects of high-temperature exposure on the phases observed in the system. TEM was used to identify the phases in both as-cast and heat-treated microstructures, and the results were compared to the thermodynamic predictions for the system. Since Fe is typically restricted due to the detrimental effect of brittle Fe intermetallics, tensile testing was performed to evaluate the effect of increasing Fe on the ductility and strength of the alloys.

II. MATERIALS AND METHODS

CALPHAD (CALculation of PHAse Diagrams) simulations were performed using Pandat thermodynamic software by CompuTherm. The PanAl2023 database was used to perform equilibrium and Scheil calculations to evaluate the Al–Ce–Fe alloy system.

Several alloys were prepared using master alloys of Al–10Ce, Al–25Fe, and commercially pure Al. The master alloys were melted in air using an induction furnace. The melts were then subjected to a 20-minute vacuum (~ 5×10^{-1} Torr) treatment for degassing before casting. A steel mold that produces plates of 5 mm × 12 mm × 150 mm, preheated to 100 °C that provides cooling rates around 35 K/s, was used to make samples suitable for tensile testing. Microstructure analysis samples were prepared using a steel cooling cup buried in insulating sand, which provides cooling rates similar to traditional sand cooling cups. Optical Emission Spectroscopy (OES) was used to measure the chemical composition of the casting samples seen in Table I. Heat treatments were performed for 120 hours at 350 °C and 500 °C followed by natural air cooling to observe the change in microstructure and the property retention after exposure to high temperatures.

From the plate castings, ASTM E8 subsize tensile bars were machined and at least three samples were tested for each condition. The tensile tests were performed on an MTS Criterion Electromechanical Universal Test System at room temperature, with a constant strain rate of 0.005 mm/s. Samples suitable for SEM were sectioned and mounted in conductive mounting material and prepared using standard metallographic techniques. SEM and EDS analyses were carried out on a FEI Apreo LoVac high-resolution electron microscope equipped with a back-scattered electron (BSE) detector operating at 10-15 kV with a current of 1.6-3.2 nA. The structure and chemical compositions of main intermetallic phases of test alloys were further characterized using TEM and scanning transmission electron microscopy (STEM) techniques. Specimens for TEM/STEM characterization were prepared using electropolishing in an electrolyte consisting of 25 pct nitric acid in methanol at − 20 °C and 20 V. Site specific TEM samples were prepared using a FEI Helios Nanolab 600 focused ion beam system. Conventional TEM imaging and electron diffraction study were conducted on a FEI Tecnai F20 microscope operating at 200 keV. Atomic resolution high angle annular dark field (HAADF) STEM imaging was performed on a Thermo Fisher S-CORR probe corrected Themis-Z microscope equipped with a quad-silicon drift detector (Super-X) operating at 300 keV.

III. RESULTS AND DISCUSSION

A. *CALPHAD Simulations*

Since the targeted processing technique is casting, the Al–Ce eutectic composition calculated at 9.35 pct Ce, which should provide good castability, was chosen for CALPHAD analysis. From the Al–9.35Ce–xFe equilibrium isopleth in Figures 1(a) and (b), the alloy is predicted to form $Al_{10}CeFe_2$ phase between 480 °C and 638 °C for any amount of Fe above the maximum solubility of 0.027 pct. At temperatures below 480 °C, the $Al_{10}CeFe_2$ phase is replaced by $Al_{13}Fe_4$ and $Al_{11}Ce_3$ binary phases. Additions of Fe up to 0.91 pct slightly increase the stability of the $Al_{11}Ce_3$ phase seen from the L + $Al_{11}Ce_3$ phase field in Figure 1(b). Fe content above 0.91 pct is predicted to form $Al_{10}CeFe_2$ phase at temperatures above Al or $Al_{11}Ce_3$, and further additions

Table I. Alloy Target and Experimental Compositions in Wt Pct Measured by OES

Alloy Target	Sample Type	Ce	Fe	Si	Zn	Others Total	Al
Al–9.35Ce	microstructure	9.43	0.05	0.14	0.26	0.22	bal.
	as-cast tensile	9.57	0.20	0.15	0.26	0.23	bal.
Al–9.35Ce−1Fe	microstructure	9.33	1.02	0.18	0.26	0.21	bal.
	as-cast + heat treatment tensile	9.45	1.16	0.16	0.26	0.27	bal.

of Fe above 2.1 pct are predicted to form $Al_{13}Fe_4$ phase at high temperatures before Al or $Al_{11}Ce_3$ or $Al_{10}CeFe_2$. Figure 1(c) is the liquidus projection for the Al–Ce–Fe system, showing several possible phases predicted to form depending on the composition. From the projection, larger additions of Ce and Fe result in a significant increase in the liquidus temperature of the alloy due to primary formation of intermetallic phases. Previous research has indicated the formation of primary or proeutectic $Al_{11}Ce_3$, which usually displays a large faceted morphology, can slightly improve the yield strength (YS) and hardness of Al–Ce binary alloys at the cost of ductility.[8,9] Previous investigations into the casting Al–Ce–Fe system showed the suspected formation of $Al_{10}CeFe_2$ supported by CALPHAD predictions, but other ternary Al–Ce–Fe phases like Al_8CeFe_2 seen in Figure 1(c) were not considered.[1,20] Additionally, the predictions did not show the possibility of low-temperature $Al_{13}Fe_4$ phase replacing the ternary $Al_{10}CeFe_2$ phase as shown in Figure 1(a).[1,20] To determine the effect of Fe on the Al–Ce binary system, Al–9.35Ce and Al–9.35Ce−1Fe alloys were chosen for testing. The compositions of the experimental alloys are shown in Table I. As a result of impurities in the Al–10Ce master alloy, Si and zinc (Zn) were present in all the samples. Due to the variability in the Fe content of the master alloys, the Al–9.35Ce alloys ended up with 0.05 pct Fe (microstructure sample) and 0.2 pct Fe (tensile samples), and the Al–9.35Ce−1Fe mechanical test sample also had slightly excess Fe at 1.16 pct. Additionally, the Ce level of the master alloy varied, resulting in most of the alloys being slightly hypereutectic. The effects of the real compositions are considered in the CALPHAD analysis.

The effect of Si impurity on the Al–9.35Ce−1Fe alloy is shown in Figure 1(d). It is predicted that Si will form ternary Al–Ce–Si phases, namely AlCeSi and $AlCeSi_2$, at high temperatures while the α-AlFeSi phase is predicted at temperatures below 250 °C. In the previous work by the current authors, the effect of 1 and 2 pct Si additions on a target Al–9Ce−1Fe alloy were shown to form a ternary Al–Ce–Si phase, which formed at the cost of the $Al_{11}Ce_3$ phase. The Si addition showed little effect on the Al–Ce–Fe ternary phase in the alloy and resulted in a significant reduction in ductility.[1,3] The previous results are consistent with the phase diagram in Figure 1(d). Therefore, it is not expected for Fe to form Al–Fe–Si intermetallics during solidification due to the stability of Al–Ce–Si intermetallics in the current Al–Ce–Fe–Si alloy system. In other Al–Si alloys, the Al–Fe–Si intermetallics that form during solidification are difficult to modify *via* heat treatment due to the low diffusivity of Fe and the stability of Al–Fe–Si at high temperatures.[7] The diffusion of Ce at low temperatures is also difficult, so it is not expected for the predicted $Al_{10}CeFe_2$ phase to transform into $Al_{13}Fe_4$ or α-AlFeSi phase at lower temperatures.[22,23] Since the Si levels for the experimental alloys are within 0.04 wt pct and Si is not expected to interact with Fe, the effect of the Si impurity was not investigated in this work.

Figure 1(e) shows the effect of the Zn impurity on the Al–9.35Ce−1Fe alloy. It is predicted that Zn will stay in solution for temperatures above 85 °C at 0.26 pct Zn, increasing to around 173 °C at 1.0 pct Zn. It is unlikely the predicted low-temperature $Zn_{11}Ce$ phase will form due to the low diffusivity of Ce in Al.[22] Zn is known to provide very little solid solution strengthening in Al,[24] and therefore, Zn alloying is usually intended for precipitation strengthening *via* thermomechanical processing in combination with other elements.[25] Meanwhile, the predicted effects of 0.26 pct Zn on the formation temperatures of $Al_{10}CeFe_2$ (0.67 °C rise), $Al_{11}Ce_3$ (0.93 °C rise), and the Al matrix (0.45 °C drop) shown in the magnified region in Figure 1(e) are negligible. Since the Zn is expected to stay in solid solution and the Zn levels in the alloys were measured to be the same, the effect of the Zn impurity was not investigated.

Scheil simulations can provide predictions for the solidification behavior under the assumption of no diffusion in solid phases but infinite diffusion in liquid phases. Scheil simulations were performed for Al–9.45Ce−0.16Si–0.26Zn with additions of 0.05, 0.2, 1.02, and 1.16 pct Fe, which represents the average experimental compositions, and the results are plotted in Figure 1(f). The solidification sequences and liquidus temperature of individual phases are provided in Table II. For the four alloys with varying Fe concentration, $Al_{10}CeFe_2$ phase is predicted to form during solidification. For the 1.02 and 1.16 pct Fe alloys, the $Al_{10}CeFe_2$ phase forms first at 656.6 °C and 665.5 °C, respectively. In the 0.05 and 0.2 pct Fe alloys, the $Al_{10}CeFe_2$ phase is predicted to form last during solidification at 633.1 °C and 634.4 °C, respectively. Since Si was included in the calculations, AlCeSi phase also appears in each alloy at around 634.7 °C to 636.8 °C, decreasing with increasing Fe content as shown in Table II. The primary Al phase is only predicted to form first at 639.1 °C in the alloy with 0.05 pct Fe with the $Al_{11}Ce_3$ phase forming less than around 0.4 °C later. In the alloy with 0.2 pct Fe, the $Al_{11}Ce_3$ phase forms first at 638.6 °C with the Al matrix forming around 0.4 °C after it, which is consistent with

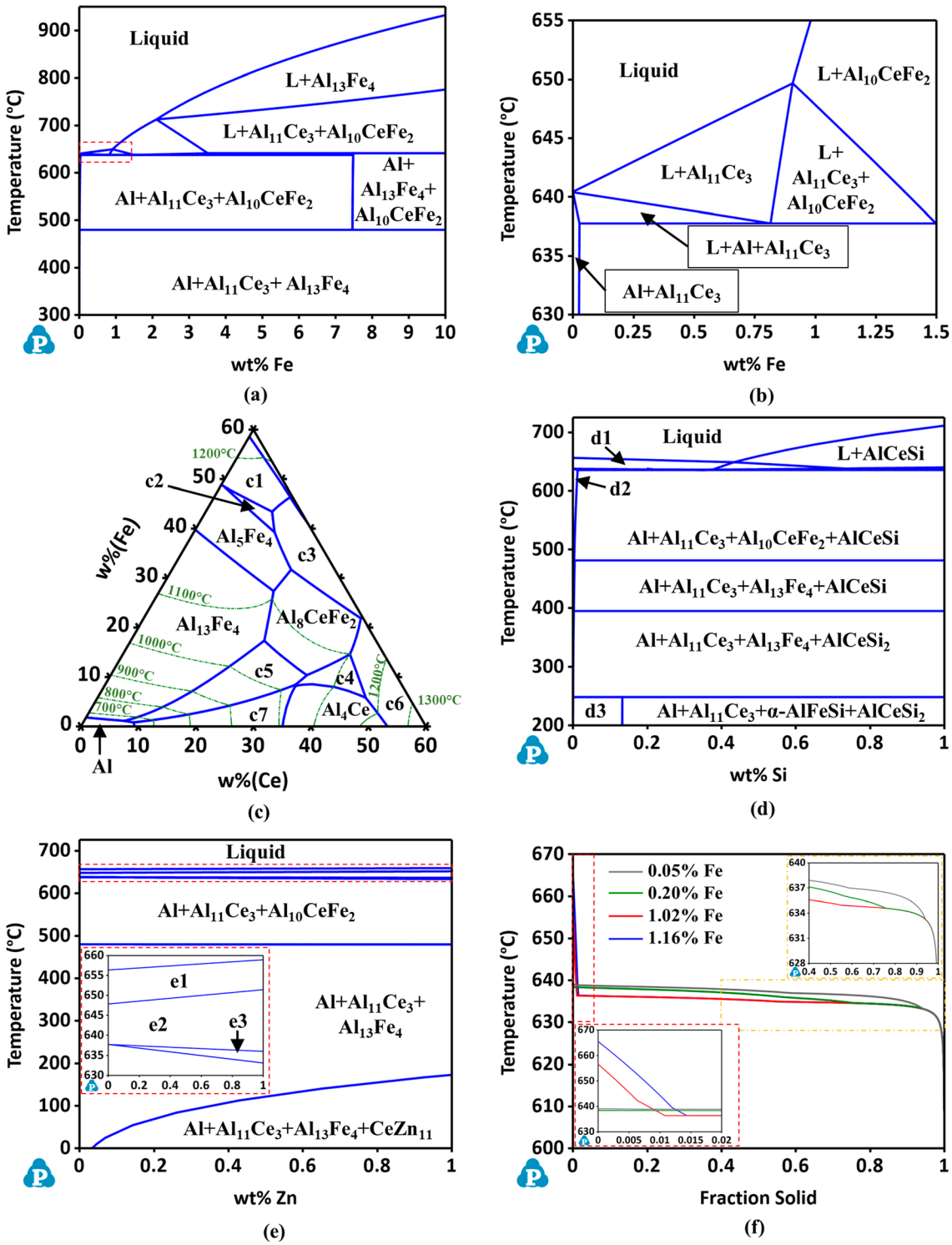


Fig. 1—(*a*) equilibrium isopleth of Al–9.35Ce–*x*Fe alloy where the dashed red box indicates the magnified region shown in (*b*). (*c*) liquidus projection in the Al-rich corner of the Al–Ce–Fe system where region c1 is Al_5Fe_2, c2 is Al_2Fe, c3 is Al_8CeFe_4, c4 is Al_3Ce, c5 is $Al_{10}CeFe_2$, c6 is Al_2Ce, and c7 is $Al_{11}Ce_3$. (*d*) equilibrium isopleth of Al–9.35Ce−1Fe–*x*Si where region d1 is L + $Al_{10}CeFe_2$, d2 is Al + $Al_{11}Ce_3$ + $Al_{10}CeFe_2$, and d3 is Al + $Al_{11}Ce_3$ + α-AlFeSi + $Al_{13}Fe_4$. (*e*) equilibrium isopleth of Al–9.35Ce−1Fe–*x*Zn with a magnified region (indicated by the dashed red box) where region e1 is L + $Al_{10}CeFe$, e2 is L + $Al_{11}Ce_3$ + $Al_{10}CeFe_2$, and e3 is L + Al + $Al_{11}Ce_3$ + $Al_{10}CeFe_2$. (*f*) Scheil simulations for Al–9.45Ce−0.16Si–0.26Zn–(0.05, 0.2, 1.02, 1.16) Fe with magnified regions at the beginning (marked by dashed red box) and end (marked by orange dash-dot box) of solidification (Color figure online).

Table II. Scheil Simulation Data Showing the Solidification Sequence, Liquidus Temperature, and Phase Fraction at the End of Solidification from Fig. 1(f)

Parameter		Fe Content (Wt Pct)			
		0.05	0.2	1.02	1.16
Solidification Sequence		$L + Al \rightarrow L + Al + Al_{11}Ce_3 \rightarrow L + Al + Al_{11}Ce_3 + AlCeSi \rightarrow L + Al + Al_{11}Ce_3 + AlCeSi + Al_{10}CeFe_2 \rightarrow Al + Al_{11}Ce_3 + AlCeSi + Al_{10}CeFe_2$	$L + Al_{11}Ce_3 \rightarrow L + Al + Al_{11}Ce_3 \rightarrow L + Al + Al_{11}Ce_3 + AlCeSi \rightarrow L + Al + Al_{11}Ce_3 + AlCeSi + Al_{10}CeFe_2 \rightarrow Al + Al_{11}Ce_3 + AlCeSi + Al_{10}CeFe_2$	$L + Al_{10}CeFe_2 \rightarrow L + Al_{11}Ce_3 + Al_{10}CeFe_2 \rightarrow L + Al + Al_{11}Ce_3 + Al_{10}CeFe_2 \rightarrow L + Al + Al_{11}Ce_3 + AlCeSi + Al_{10}CeFe_2 \rightarrow Al + Al_{11}Ce_3 + AlCeSi + Al_{10}CeFe_2$	
Al	Liquidus Temp. (°C)	639.1	638.2	636.2	636.2
	Phase Fraction (Pct)	90.93	90.62	88.79	88.48
$Al_{11}Ce_3$	Liquidus Temp. (°C)	638.7	638.6	642.2	639.2
	Phase Fraction (Pct)	8.480	8.320	7.360	7.190
$Al_{10}CeFe_2$	Liquidus Temp. (°C)	633.1	634.4	656.6	665.5
	Phase Fraction (Pct)	0.15	0.63	3.41	3.89
AlCeSi	Liquidus Temp. (°C)	636.8	635.8	634.8	634.7
	Phase Fraction (Pct)	0.44	0.44	0.44	0.44
Total Intermetallic Fraction (Pct)		9.07	9.39	11.21	11.52

the isopleth seen in Figure 1(b). No Zn phases appeared during the solidification simulation.

The phase fractions of at the end of the Scheil simulation are provided in Table II. From the table, only a small fraction of AlCeSi phase (0.44 pct) is predicted in the alloys with around 0.16 pct Si impurity in the present work. The amount of $Al_{10}CeFe_2$ phase increases with increasing Fe content from 0.15 at 0.05 pct Fe to 3.89 pct at 1.16 pct Fe, while the amount of the Al matrix, $Al_{11}Ce_3$, and AlCeSi phases decreases. The total predicted intermetallic fraction increases by 2.45 pct as a result of the of increasing the Fe content from 0.05 and 1.16 pct in the alloy.

B. *As-Cast Microstructure Results*

Representative microstructures of the as-cast Al–9.35Ce and Al–9.35Ce−1Fe alloys are shown in Figure 2. The Al–9.35Ce alloy microstructure shown in Figure 2(a) consists mostly of Al–$Al_{11}Ce_3$ eutectic structure, some proeutectic $Al_{11}Ce_3$ particles that are coarse and faceted, and a limited number of Al dendrites not shown in Figure 2(a). The observed microstructure is consistent with the measured composition (9.43 pct Ce) close to the calculated eutectic point of the alloy and similar to the microstructures of near-eutectic Al–Ce alloys in literature.[8,20] The faceted proeutectic $Al_{11}Ce_3$ phase usually appears with similar morphology as the one shown in Figure 2(a) and was observed to be as large as 500 μm in length in the Al–9.35Ce microstructure sample.

From the as-cast microstructure of the Al–9.35Ce−1Fe target alloy in Figure 2(c), a ternary Al–Ce–Fe phase forms in the alloy with 1 pct Fe during solidification, confirmed by SEM-EDS spot analysis (average 78.7 at. pct Al, 6.8 at. pct Ce, 8.2 at. pct Fe), while faceted proeutectic $Al_{11}Ce_3$ formation was suppressed. Although there were some proeutectic $Al_{11}Ce_3$ particles seen in the microstructure of the Al–9.35Ce−1Fe not shown in Figure 2(c), the amount was reduced to a few individual instances compared to the samples without Fe addition. In most areas of the microstructure, such as that shown in Figures 2(c) and (d), separate colonies of $Al_{11}Ce_3$ eutectic phase and the Al–Ce–Fe phase could be seen while the phases were mixed in other areas. According to the Scheil data in Table II, the onset temperature for the $Al_{11}Ce_3$ phase and the predicted $Al_{10}CeFe_2$ phase are around 14 °C apart, but the formation temperature of the observed Al–Ce–Fe phase is unknown. From the cast microstructures in the Al–9.35Ce−1Fe target alloy, both the $Al_{11}Ce_3$ and Al–Ce–Fe phase were refined. This indicates that the observed Al–Ce–Fe phase likely did not form at significantly higher temperatures, allowing for coarsening commonly seen in other Al cast alloys with high Fe content.[6] It is possible the driving force for $Al_{11}Ce_3$ formation was decreased due to the Al–Ce–Fe phase formation around the same temperatures, which explains the suppression of the proeutectic $Al_{11}Ce_3$.

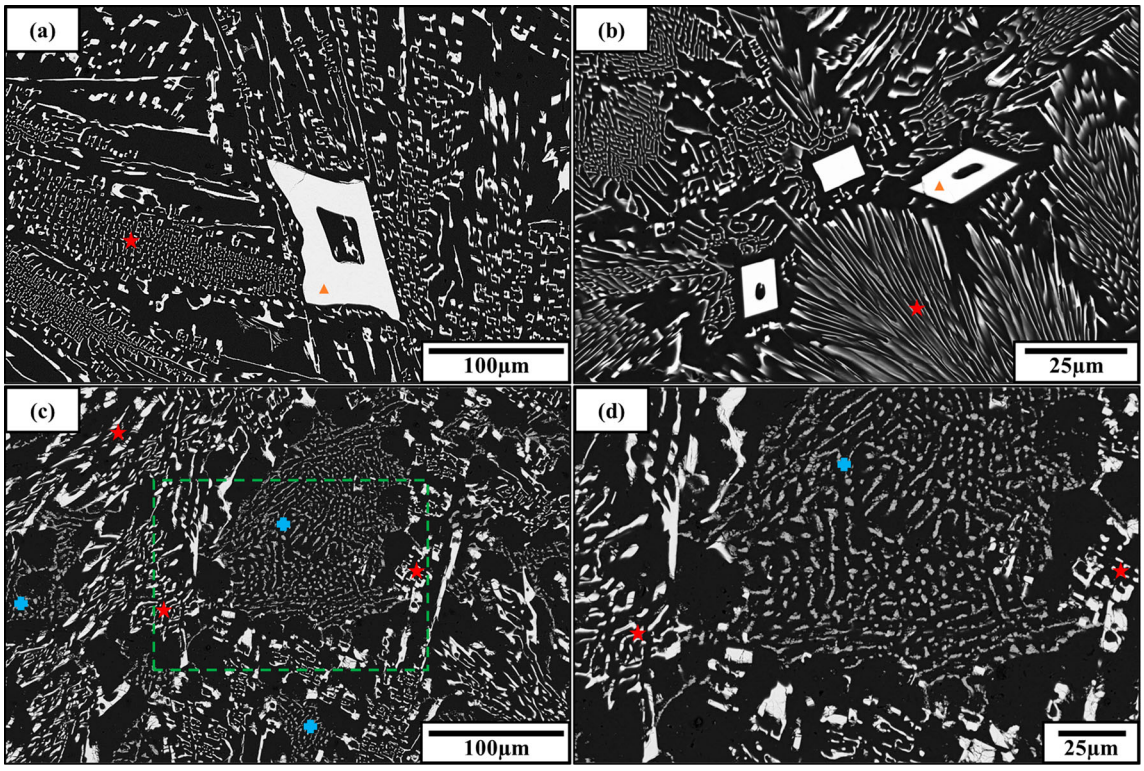
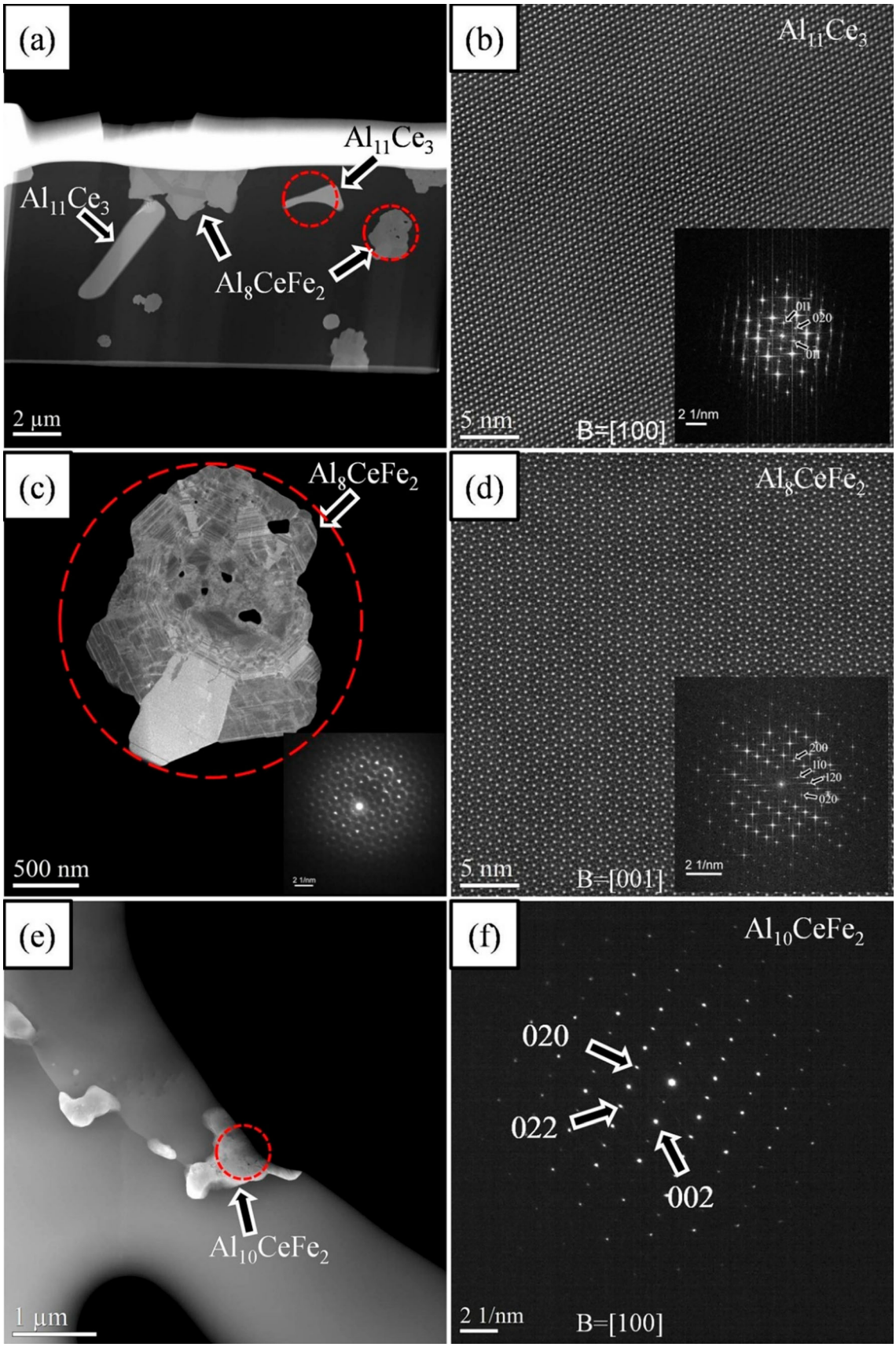


Fig. 2—SEM BSE microstructure images of as-cast microstructure samples for the (*a*) Al–9.35Ce and (*c*, *d*) Al–9.35Ce−1Fe alloys. (*b*) microstructure from the Al–9.35Ce tensile sample. (*d*) shows a higher magnification of the area indicated by the dashed green box in (*c*). Eutectic $Al_{11}Ce_3$ phase is marked by red stars, proeutectic $Al_{11}Ce_3$ is marked by orange triangles, and Al_8CeFe_2 phase is marked by a blue '+' (Color figure online).


(a)
$Al_{11}Ce_3$
$Al_{11}Ce_3$
Al_8CeFe_2
2 μm
(b)
$Al_{11}Ce_3$
011
020
011
5 nm
B=[100]
2 1/nm
(c)
Al_8CeFe_2
500 nm
2 1/nm
(d)
Al_8CeFe_2
200
110
120
020
5 nm
B=[001]
2 1/nm
(e)
$Al_{10}CeFe_2$
1 μm
(f)
$Al_{10}CeFe_2$
020
022
002
2 1/nm
B=[100]

◀Fig. 3—STEM characterization of intermetallic phases in as-cast Al–9.3Ce−1Fe alloy: (*a*) low magnification HAADF-STEM image. The red dashed circles highlight the regions for atomic resolution imaging of $Al_{11}Ce_3$ in (*b*) and Al_8CeFe_2 in (*d*), respectively. (*b*) atomic resolution HAADF-STEM image of $Al_{11}Ce_3$ phase along its [100] zone axis with the inserted corresponding FFT pattern. (*c*) HAADF-STEM image of an Al_8CeFe_2 aggregate with an inserted electron diffraction showing the pseudo-tenfold symmetry. The red circle highlights the aggregate for the selected area diffraction study. (*d*) atomic resolution HAADF-STEM image of Al_8CeFe_2 phase along its [001] zone axis with the inserted corresponding FFT pattern. (*e*) HAADF-STEM image of $Al_{10}CeFe_2$ phase. The red dashed circle highlights the region for selected area electron diffraction study in (*f*). (*f*) selected area electron diffraction pattern along [100] zone axis of $Al_{10}CeFe_2$ phase (Color figure online).

The SEM-EDS measured composition was not close to the predicted composition of $Al_{10}CeFe_2$ phase, so TEM was performed to verify the composition and identify the crystal structure of the phase inferred in SEM. Figure 3(a) is a HAADF-STEM image showing the microstructure of Al–9.35Ce−1Fe alloy. Two main intermetallic phases, $Al_{11}Ce_3$ and Al_8CeFe_2, were identified in the microstructure. $Al_{11}Ce_3$ phase has an orthorhombic crystal structure (space group Immm, lattice parameters: a = 0.43696 nm, b = 1.2966 nm, c = 1.00979 nm[26]). The structure of $Al_{11}Ce_3$ phase is the same as that of Al_4Ce phase reported in a previous study.[17] Figure 3(b) is a [100] zone axis atomic resolution HAADF-STEM image of $Al_{11}Ce_3$ phase along with the indexed Fast Fourier Transform (FFT) pattern. Al_8CeFe_2 phase has an orthorhombic crystal structure (space group Pbam, lattice parameters: a = 1.24867 nm, b = 1.4281 nm, c = 0.40387 nm[27]). Al_8CeFe_2 phase often has aggregate structures, consisting of multiple twin grains. An example of this structure is shown in Figure 3(c). The inserted electron diffraction pattern of the Al_8CeFe_2 aggregate exhibits pseudo-tenfold symmetry. A [001] zone axis atomic resolution HAADF-STEM image of Al_8CeFe_2 along with the indexed FFT pattern is shown in Figure 3(d).

Equilibrium $Al_{10}CeFe_2$ phase was also observed in the as-cast microstructure. $Al_{10}CeFe_2$ phase has an orthorhombic crystal structure (space group Cmcm, lattice parameters: a = 0.87508 nm, b = 0.99818 nm, c = 0.880902 nm[28,29]). $Al_{10}CeFe_2$ found in the current study has a different crystal structure and lattice parameter as compared with the metastable $Al_{10}CeFe_2$ phase reported in the previous study[17]; however, the observed $Al_{10}CeFe_2$ phase in the current study has the same crystal structure and similar lattice parameters of $Al_{13}Fe_3Ce$ phase reported in the same study[17].Figure 3(e) shows $Al_{10}CeFe_2$ phase in the as-cast microstructure. Its corresponding selected area diffraction pattern is given in Figure 3(f). The compositions of three phases in the as-cast Al–9.35Ce−1Fe alloy, measured using STEM-EDS analysis, are summarized in Table III and show limited solubility of Fe in the $Al_{11}Ce_3$ phase, indicating that the $Al_{11}Ce_3$ phase will not act as a Fe sink in aluminum alloys. The STEM-EDS measured composition of the Al_8CeFe_2 phase is in good agreement with the ideal atomic composition for the phase, while the SEM-EDS results showed composition considerably lower in Fe content, indicating low reliability with SEM measurements.

Table III. Chemical Composition in Atomic Percent of Main Intermetallic Phases from the Al–9.3Ce−1Fe Microstructure Sample Measured Using STEM-EDS

Phase	Al	Ce	Fe	Si	Zn
$Al_{11}Ce_3$	77.6	21.29	0.55	0.42	0.14
Al_8CeFe_2	71.01	7.83	19.50	1.63	0.03
$Al_{10}CeFe_2$	72.7	10.55	16.7	0	0.05
$CeAl_{0.85}Si_{1.15}$	25.9	42.5	3	28.5	0.1

It is noted that most of the Al–Ce–Fe ternary phases formed were the Al_8CeFe_2 phase, which is interesting considering that Al_8CeFe_2 is predicted at much higher Fe (> 13 pct) and Ce (> 20 pct) concentrations from the liquidus projection in Figure 1(c). It is possible that during solidification, non-equilibrium kinetics promoted the formation of Al_8CeFe_2. The Al_8CeFe_2 phase exhibits both small globular and small plate-like morphology as seen in Figure 2(d). The $Al_{10}CeFe_2$ phase observed by TEM in the current study was located at the grain boundaries, indicating it formed later during solidification. The as-cast microstructure of the Al–9.35Ce−1Fe target alloy is similar to the recently investigated as-cast Al–10Ce−1Fe alloy,[20] which used SEM-EDS to infer the Al–Ce–Fe phase as predicted $Al_{10}CeFe_2$. In both cases, the $Al_{11}Ce_3$ phase appears as the bright high-contrast phase, while the Al–Ce–Fe phase (inferred as Al_8CeFe_2 in the current work) appears as dull gray.

Since the tensile samples were made using a permanent mold, the microstructure was investigated to determine the effect of the faster cooling rate on the alloys compared to the microstructure samples shown in Figures 2(a) and (b). Figure 2(b) shows an example microstructure of the Al–9.35Ce target alloy from the tensile casting conditions. The microstructures of the tensile castings are similar to the microstructure castings, with a more refined microstructure as shown in Figure 2(b) compared to Figure 2(a).

C. *Effect of Heat Treatment on Microstructure*

Since target applications of Al–Ce alloys may involve exposure to elevated temperatures for extended periods during operation, observation of the microstructure after heat treatment/exposure is necessary. The Al–9.35Ce−1Fe microstructure sample was treated at 350 °C and 500 °C (> 75 pct of predicted liquidus temperature) for 5 days (120 hours), which is similar to an investigation of the Al–Ce binary system that used 500 °C for 7 days (168 hours).[8] Heat treatment at 350 °C was chosen to determine if the Al_8CeFe_2 phase seen in the as-cast microstructure would transform into the low-temperature equilibrium $Al_{13}Fe_4$ and $Al_{11}Ce_3$ phases, as predicted in Figure 1(a). Meanwhile, the 500 °C heat treatment was selected to determine if the

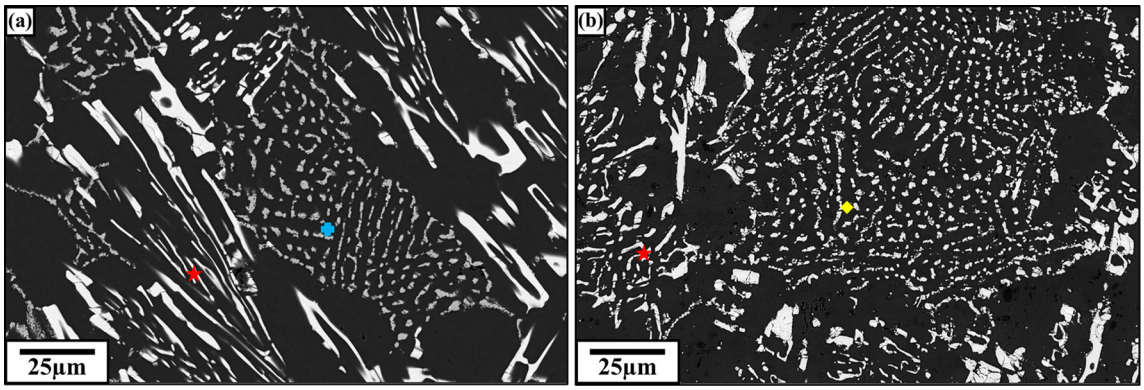


Fig. 4—SEM BSE microstructure images after 120 hours at 350°C (*a*) and 500°C (*b*) of Al–9.35Ce−1Fe microstructure sample. Eutectic $Al_{11}Ce_3$ phase is marked by red stars, Al_8CeFe_2 phase is marked by a blue '+,' and $Al_{10}CeFe_2$ is marked by a yellow diamond (Color figure online).

as-cast Al_8CeFe_2 phase would transform into the high-temperature equilibrium $Al_{10}CeFe_2$.

The microstructures of the samples after heat treatment are shown in Figure 4. SEM analysis of the Al–9.35Ce−1Fe sample heat-treated at 350 °C for 120 hours revealed no intermetallic coarsening or phase changes occurred as a result of the exposure. Seen in Figure 4(a), the Al–Ce–Fe phase appears as dull gray like the as-cast microstructure shown in Figure 2(c) and (d) with similar SEM-EDS spot analysis as the as-cast Al_8CeFe_2 phase (average 82.7 at. pct Al, 6.1 at. pct Ce, 11.2 at. pct Fe). The results of the 350 °C exposure indicate that the limited mobility of Fe and Ce hinders the predicted equilibrium phase transformations (Al_8CeFe_2 to $Al_{11}Ce_3$ and $Al_{13}Fe_4$). Figure 4(b) shows the SEM micrograph after heat treatment at 500 °C for 120 hours, which was observed from the same area as the as-cast sample in Figure 2(d). From Figure 4(b), there is no evidence of coarsening of intermetallic phases during the 500 °C heat treatment, but minor differences in the microstructure after the heat treatment are apparent. In Figure 4(b), the contrast of the Al–Ce–Fe ternary phase is less apparent than in the as-cast microstructure (Figure 2(d)). However, the SEM-EDS spot analysis showed that the composition of the Al–Ce–Fe phase (average 85.9 at. pct Al, 7.2 at. pct Ce, 7.0 at. pct Fe) was similar to the as-cast microstructure.

The main phases in the Al–9.35Ce−1Fe alloy after heat treatment at 500 °C include $Al_{11}Ce_3$ and $Al_{10}CeFe_2$ phase. Figure 5(a) is a bright-field STEM image showing the $Al_{10}CeFe_2$ phase in the heat-treated microstructure. The Al_8CeFe_2 phase in the as-cast microstructure transformed into the predicted equilibrium $Al_{10}CeFe_2$ phase during the heat treatment. The Al–9.35Ce−1Fe alloy shows minimal coarsening of the $Al_{11}Ce_3$ phase which is consistent with other studies.[8] The results indicate that the intermetallic phases are sufficiently resistant to coarsening in comparison to other works,[8,10] and thus, the alloy is expected to have similar property retention at elevated temperatures.

Since there was Si impurity in the alloys, TEM characterization revealed the formation of $CeAl_{0.85}Si_{1.15}$ phase, with a tetragonal crystal structure (space group I 41/a m d) and lattice parameters a = 0.4203 nm, b = 0.4203 nm, and c = 1.44619 nm.[30] Figure 5(c) shows $CeAl_{0.85}Si_{1.15}$ phase in the microstructure, and the corresponding diffraction pattern is given in Figure 5(d). The composition of $CeAl_{0.85}Si_{1.15}$ phase was measured using STEM-EDS and listed in Table III. No interaction between Si and Fe was observed in the experimental alloys, supporting the CALPHAD results in Figures 1(d) and (f) and previous findings.[1,3]

According to the isopleth in Figure 1(a), the $Al_{14}Fe_3$ and $Al_{11}Ce_3$ phases are stable at temperatures less than 480 °C, but the Al–9.35–1Fe alloy treated at 350 °C for 120 hours in the current work and the cast Al–10Ce−1Fe alloy treated at 400 °C for 384 hours reported in literature[20] did not exhibit a phase change after treatment. The combined results show that the as-cast Al_8CeFe_2 phase identified in this work is difficult to transform into the two binary phases, even at elevated temperatures (around 200 °C higher than normal use temperatures for aluminum[22]) for considerable lengths of time, indicating the microstructure stability of the alloy. At temperatures above 480 °C, the $Al_{10}CeFe_2$ phase is stable, which was found in the Al–9.35Ce−1Fe alloy treated at 500 °C in this work. The contrast difference between the $Al_{11}Ce_3$ phase of the Al–Ce–Fe phase decreases noticeably due to the change in composition of the phase according to Table III as seen in Figure 4(b) compared to Figure 2(d). The Al–10Ce−1Fe alloy in literature[20] was treated at 590 °C for only 24 hours and also appears to show a contrast change of the Al–Ce–Fe phase that makes it more difficult to differentiate between the $Al_{11}Ce_3$ and Al–Ce–Fe phase. Although no phase change was reported by the authors, it is likely that Al_8CeFe_2 phase formed in the as-cast microstructure but transformed to $Al_{10}CeFe_2$ phase in the Al–10Ce−1Fe alloy similar to the results in the current work.

D. *Mechanical Property Testing*

The alloys evaluated in this investigation were not designed for high mechanical properties, but rather to evaluate the effect of the Fe addition on the mechanical properties (mostly ductility) of the cast Al–Ce alloys.

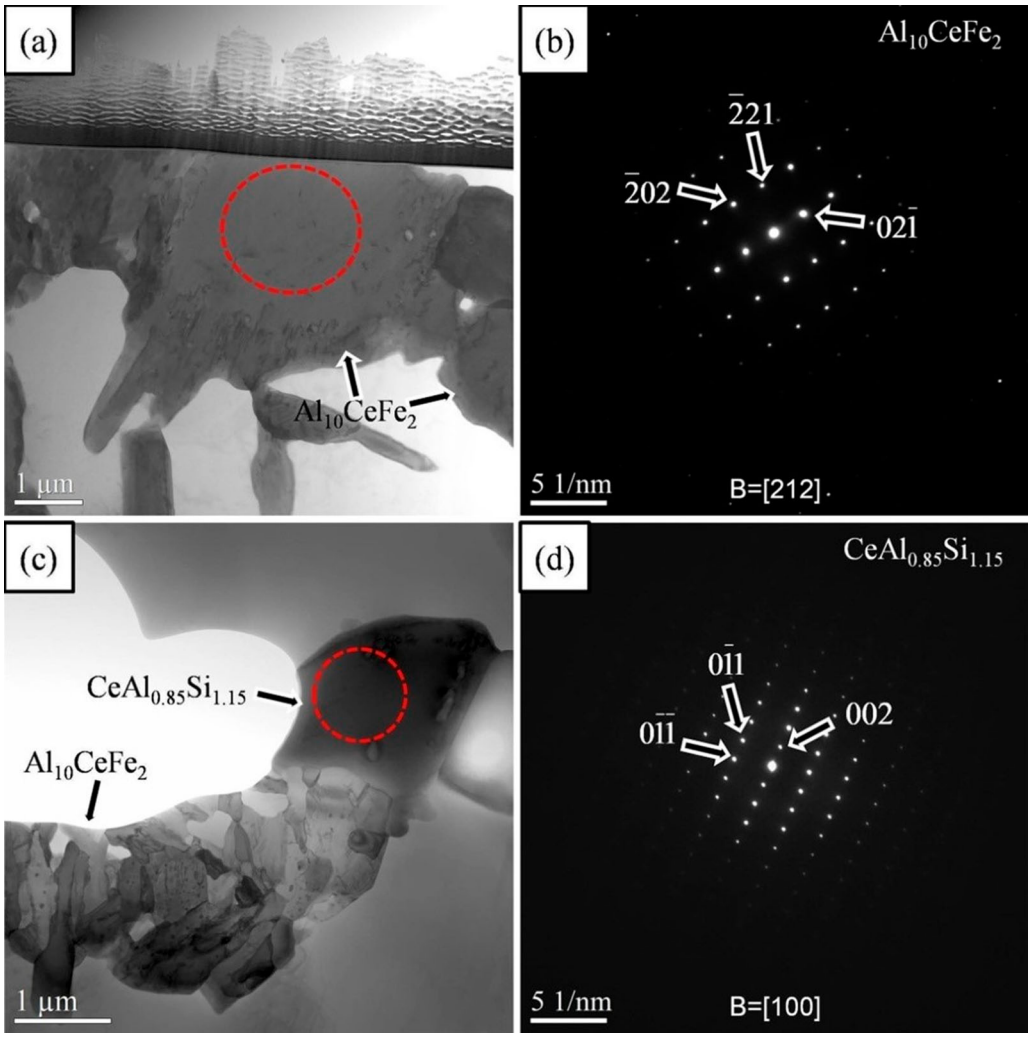


Fig. 5—STEM characterization of the microstructure of Al–9.3Ce−1Fe alloy after heat treatment: (*a*) low magnification bright-field STEM image of $Al_{10}CeFe_2$ phase. The red dashed circle highlights the region for selected area electron diffraction study in (*b*). (b) indexed selected area electron diffraction pattern along the [212] zone axis of $Al_{10}CeFe_2$ phase. (*c*) bright-field STEM image of $CeAl_{0.85}$ $Si_{1.15}$ phase. The red dashed circle highlights the region for selected area electron diffraction study in (*d*). (d) indexed selected area electron diffraction pattern along the [100] zone axis of $CeAl_{0.85}Si_{1.15}$ (Color figure online).

The results from the tensile testing are shown in Table IV. Compared to the Al–9.57Ce−0.2Fe sample, the Al–9.45Ce−1.16Fe sample showed a similar ultimate tensile strength (UTS), 12 pct larger YS, and a 25 pct larger elongation at failure. The increased elongation is believed to be related to the suppression of the faceted $Al_{11}Ce_3$ phase with the increased Fe content. The reason for the increase in YS is unknown, but potential causes could be an increased amount of Fe that stays in the Al matrix (solution) during solidification or from an increase in the total intermetallic fraction from the higher Fe content. The results from the Al–9.57Ce−0.2Fe and Al–9.45Ce−1.16Fe alloys clearly show a beneficial effect of Fe addition on the ductility and strength of the as-cast alloy, as opposed to typical effects of Fe in other cast aluminum alloys, especially those based in Al–Si systems.

It is important to understand if the high-temperature exposure embrittles the alloy. Tensile samples heat-treated at 500 °C were tested at room temperature. Due to material availability and previous study on the binary Al–Ce system[8] and Al–Ce–Fe system[20] only Al–9.45Ce−1.16Fe tensile samples were prepared for heat treatment. The results in Table IV indicate that the heat treatment had a positive effect on the elongation (30 pct increase) of the alloy compared to the as-cast alloy, suggesting that the transition of Al_8CeFe_2 to $Al_{10}CeFe_2$ phase is not embrittling. Meanwhile, 86 pct of the UTS was retained, and the YS had a retention of 90 pct. The loss of YS could be explained by Fe leaving solution at high temperatures to form the Al–Ce–Fe intermetallics, which is supported by the similar YS of the as-cast Al–9.57Ce−0.2Fe alloy. An analysis on cast aluminum alloys (206, 319, 356, A356, A356 + 0.5Cu)

Table IV. Room Temperature Mechanical Properties of Experimental Alloys

Alloy	Condition	Yield Strength (MPa)	Ultimate Tensile Strength (MPa)	Pct Elongation
Al–9.57Ce–0.2Fe	As-cast	64 ± 1.6	175 ± 4.8	8 ± 2.4
Al–9.45Ce–1.16Fe	As-cast	72 ± 1.6	168 ± 11.3	10 ± 1.5
	After 500 °C for 120 hours	64 ± 3.4	145 ± 3.8	13 ± 2.7

for potential use as cylinder heads (in T6 or T7 condition) showed less than 60 pct retention in hardness after 200 hours of exposure at 300 °C for the aged alloys. Notably, the 356 alloy, which has considerably higher Fe (0.39 pct Fe) than the A356 alloy (0.18 pct Fe), showed a higher hardness retention.[31]

IV. CONCLUSIONS

The effects of Fe additions to the near-eutectic Al–9.35Ce casting alloy have been investigated in this work using CALPHAD modeling and experimental validation. SEM and TEM were used to characterize the microstructure and tensile testing was performed to evaluate the mechanical properties. The effect of 120 hours of exposure at 350 °C and 500 °C was also evaluated, and the results are summarized:

1. Fe addition to Al–9.35Ce alloy resulted in the formation of metastable Al_8CeFe_2 phase during solidification, suppressing faceted proeutectic $Al_{11}Ce_3$ particles in as-cast Al–9.35Ce alloy. Metastable Al_8CeFe_2 phase exhibits aggregate morphology. The predicted equilibrium $Al_{10}CeFe_2$ phase was also observed in the as-cast microstructure.
2. Fe and Si were not found to interact and form intermetallic phases together in the Al–Ce–Fe–Si system despite the stability of Al–Fe–Si intermetallics in other systems. $CeAl_{0.85}Si_{1.15}$ was found instead in the solidification microstructure.
3. No changes in the microstructure of Al–9.35Ce–1Fe alloy were observed after heat treatment at 350 °C, suggesting thermal stability of the non-equilibrium Al_8CeFe_2 phase. No coarsening occurred after 500 °C exposure, but the Al_8CeFe_2 phase transformed to equilibrium $Al_{10}CeFe_2$ phase.
4. The mechanical property results showed an increase in strength and ductility with Fe addition to the Al–9.35Ce as-cast alloy, which is opposite of the effects of Fe on traditional Al–Si-based cast alloys.
5. The Al–9.35Ce–1Fe alloy displayed excellent retention of properties after exposure to high temperatures (90 pct retention of YS, 86 pct retention of UTS, 130 pct retention of elongation at failure) and confirmed that the transition of Al_8CeFe_2 to $Al_{10}CeFe_2$ was not embrittling.
6. Alloying with Fe may be beneficial for the Al–Ce system due to its low-cost, beneficial effects on mechanical properties and microstructure stability. Further optimization of Al–Ce–Fe alloys is needed to increase the ranges of achievable mechanical properties with favorable microstructures. This beneficial effect of Fe also opens the door for high recyclability rates and use of sorted scrap aluminum in Al-Ce-based alloy production, which would offer enormous environmental and economic benefits for manufacturing aluminum–cerium casting alloys.

ACKNOWLEDGMENTS

This material is based upon work supported by the US Department of Energy's Office of Energy Efficiency and Renewable Energy (EERE) under the Advanced Manufacturing Office Award Number DE-EE0007897, awarded to The REMADE Institute, a division of Sustainable Manufacturing Innovation Alliance Corp. This report was prepared as an account of work sponsored by an agency of the United States Government. Neither the United States Government nor any agency thereof, nor any of their employees, makes any warranty, express or implied, or assumes any legal liability or responsibility for the accuracy, completeness, or usefulness of any information, apparatus, product, or process disclosed, or represents that its use would not infringe privately owned rights. Reference herein to any specific commercial product, process, or service by trade name, trademark, manufacturer, or otherwise does not necessarily constitute or imply its endorsement, recommendation, or favoring by the United States Government or any agency thereof. The views and opinions of authors expressed herein do not necessarily state or reflect those of the United States Government or any agency thereof.

AUTHOR CONTRIBUTIONS

MM: conceptualization, methodology, investigation, validation, and writing original draft preparation; EC: conceptualization, methodology, and investigation; JM: characterization testing, investigation, writing review, and editing; AL: conceptualization, investigation, resources, writing review and editing, and supervision.

DATA AVAILABILITY

All data are available upon request. Please submit your request to the corresponding author.

CONFLICT OF INTEREST

The authors declare no competing interest.

OPEN ACCESS

This article is licensed under a Creative Commons Attribution 4.0 International License, which permits use, sharing, adaptation, distribution and reproduction in any medium or format, as long as you give appropriate credit to the original author(s) and the source, provide a link to the Creative Commons licence, and indicate if changes were made. The images or other third party material in this article are included in the article's Creative Commons licence, unless indicated otherwise in a credit line to the material. If material is not included in the article's Creative Commons licence and your intended use is not permitted by statutory regulation or exceeds the permitted use, you will need to obtain permission directly from the copyright holder. To view a copy of this licence, visit http://creativecommons.org/licenses/by/4.0/.

REFERENCES

1. M. Moodispaw, E. Cinkilic, A.A. Luo, C. Zhang, and F. Zhang: *NADCA Die Cast. Congr.*, 2022, vol. 2022, pp. 1–7.
2. WO/2022/182937: 2022.
3. A. Luo and E. Cinkilic: *Development of New Cost-Effective Methods for Removing Trace Contaminants in Recycled Materials*, 2020.
4. F. Czerwinski: *J. Mater. Sci.*, 2020, vol. 55, pp. 24–72.
5. R.T. Nguyen, D.D. Imholte, O.R. Rios, D. Weiss, Z. Sims, E. Stromme, and S.K. McCall: *Resour. Conserv. Recycl.*, 2019, vol. 144, pp. 340–49.
6. E. Cinkilic, C.D. Ridgeway, X. Yan, and A.A. Luo: *Metall. Mater. Trans. A*, 2019, vol. 50A, pp. 5945–56.
7. J.A. Taylor: *Procedia Mater. Sci.*, 2012, vol. 1, pp. 19–33.
8. F. Czerwinski: *Mater. Sci. Eng. A*, 2021, vol. 809, 140973.
9. D. Weiss: in *Advanced Casting Technologies*, InTech, 2018, p. 13.
10. D. Weiss: *J. Mater. Eng. Perform.*, 2019, vol. 28, pp. 1903–908.
11. H.B. Henderson, J.A. Hammons, A.A. Baker, S.K. McCall, T.T. Li, A. Perron, Z.C. Sims, R.T. Ott, F. Meng, M.J. Thompson, D. Weiss, and O. Rios: *Mater. Des.*, 2021, vol. 209, 109988.
12. A. Plotkowski, K. Sisco, S. Bahl, A. Shyam, Y. Yang, L. Allard, P. Nandwana, A.M. Rossy, and R.R. Dehoff: *Acta Mater.*, 2020, vol. 196, pp. 595–608.
13. M. Yi, P. Zhang, C. Yang, P. Cheng, S. Guo, G. Liu, and J. Sun: *Scr. Mater.*, 2021, vol. 198, 113838.
14. N.A. Belov, E.A. Naumova, and D.G. Eskin: *Mater. Sci. Eng. A*, 1999, vol. 271, pp. 134–42.
15. D.R. Manca, A.Y. Churyumov, A.V. Pozdniakov, A.S. Prosviryakov, D.K. Ryabov, A.Y. Krokhin, V.A. Korolev, and D.K. Daubarayte: *Met. Mater. Int.*, 2019, vol. 25, pp. 633–40.
16. F.W. Gschneider, K. A. Jr., Calderwood: *Bull. Alloys Phase Diagr.*, 1988, vol. 9, pp. 669–72.
17. R. Ayer, R.R. Mueller, J.C. Scanlon, and C.F. Klein: *Metall. Trans. A*, 1988, vol. 19A, pp. 1645–56.
18. M.L. Öveçoglu, C. Suryanarayana, and W.D. Nix: *Metall. Mater. Trans. A*, 1996, vol. 27A, pp. 1033–41.
19. L.C. Zhang, A.Q. He, H.Q. Ye, C. Huang, and Y.C. Zhang: *J. Mater. Sci.*, 2002, vol. 37, pp. 5183–89.
20. H.S. Park, C.N. Ekaputra, and D.C. Dunand: *Mater. Sci. Eng. A*, 2023, vol. 882, 145409.
21. G. Luo, X. Zhou, C. Li, J. Du, and Z.H. Huang: *Trans. Nonferrous Met. Soc. China*, 2022, vol. 32, pp. 1781–94.
22. F. Czerwinski: *Materials (Basel)*, 2020, vol. 13, pp. 1–49.
23. E. Cinkilic, M. Moodispaw, J. Zhang, J. Miao, and A.A. Luo: *Metall. Mater. Trans. A*, 2022, vol. 53A, pp. 2861–73.
24. T. Uesugi and K. Higashi: *Proceedings of the 12th International Conference on Aluminium Alloys*, 2010, pp. 1421–25.
25. L. Li, S. Ji, Q. Zhu, Y. Wang, X. Dong, W. Yang, S. Midson, and Y. Kang: *Metall. Mater. Trans. A*, 2018, vol. 49A, pp. 3247–56.
26. C. Tang, Y. Du, H.H. Xu, W. Xiong, L.J. Zhang, F. Zheng, and H.Y. Zhou: *Intermetallics*, 2008, vol. 16, pp. 432–39.
27. M. Kolenda, M.D. Koterlin, M. Hofmann, B. Penc, A. Szytuła, A. Zygmunt, and J. Ukrowski: *J. Alloys Compd.*, 2001, vol. 327, pp. 21–26.
28. S.C. Chen and C.S. Lue: *Phys. Rev. B.* https://doi.org/10.1103/PhysRevB.81.075113.
29. Y. Kawamura, J. Hayashi, K. Takeda, C. Sekine, H. Tanida, M. Sera, and T. Nishioka: *J. Phys. Soc. Jpn.*, 2016, vol. 85, pp. 1–7.
30. S. Bobev, P.H. Tobash, V. Fritsch, J.D. Thompson, M.F. Hundley, J.L. Sarrao, and Z. Fisk: *J. Solid State Chem.*, 2005, vol. 178, pp. 2091–103.
31. S. Roy, L.F. Allard, A. Rodriguez, W.D. Porter, and A. Shyam: *Metall. Mater. Trans. A*, 2017, vol. 48A, pp. 2543–62.

Publisher's Note Springer Nature remains neutral with regard to jurisdictional claims in published maps and institutional affiliations.